

1 **Turbulence Measurements from Compliant Moorings - Part II: Motion**

2 **Correction**

3 Levi F. Kilcher*

4 *National Renewable Energy Laboratory, Golden, Colorado, USA*

5 Jim Thomson

6 *Applied Physics Laboratory, University of Washington, Seattle, Washington, USA*

7 Samuel Harding

8 *Pacific Northwest National Laboratory, Richland, Washington, USA*

9 Sven Nylund

10 *Nortek AS, Norway*

11 *Corresponding author address: Levi Kilcher, National Renewable Energy Laboratory, 15013 Den-
12 ver West Pkwy, Golden, Colorado, USA

13 E-mail: Levi.Kilcher@nrel.gov

ABSTRACT

Acoustic Doppler velocimeters (ADVs) are a valuable tool for making high-precision measurements of turbulence, and moorings are a convenient and ubiquitous platform for making many kinds of measurements in the ocean. However, because of concerns that mooring motion can contaminate turbulence measurements and acoustic Doppler profilers are relatively easy to deploy, ADVs are not frequently deployed from moorings. This work demonstrates that inertial motion measurements can be used to reduce motion-contamination from moored ADV velocity measurements. Three distinct mooring platforms were deployed in a tidal channel with inertial-motion-sensor-equipped ADVs. In each case, the motion correction based on the inertial measurements dramatically reduced contamination from mooring motion. The spectra from these measurements have a shape that is consistent with other measurements in tidal channels, and have a $f^{-5/3}$ slope at high frequencies—consistent with Kolmogorov’s theory of isotropic turbulence. Motion correction also improves estimates of cross spectra and Reynold’s stresses. Comparison of turbulence dissipation with flow speed and turbulence production indicates a bottom boundary layer production-dissipation balance during ebb and flood that is consistent with the strong tidal forcing at the site. These results indicate that inertial-motion-sensor-equipped ADVs are a valuable new tool for measuring turbulence from moorings.

³⁴ **1. Introduction**

³⁵ Acoustic Doppler velocimeters (ADVs) have been used to make high-precision measurements of
³⁶ water velocity for over 20 years (Kraus et al. 1994; Lohrmann et al. 1995). During that time, they
³⁷ have been deployed around the world to measure turbulence from a range of platforms, including
³⁸ the laboratory setting (Voulgaris and Trowbridge 1998), from stationary structures on ocean-, river-
³⁹ and lake-bottoms (Kim et al. 2000; Lorke 2007; Cartwright et al. 2009), in surface waters from
⁴⁰ a pole lowered from a ship's bow (Geyer et al. 2008), and in the deep ocean from autonomous
⁴¹ underwater vehicles (e.g., Zhang et al. 2001; Goodman et al. 2006).

⁴² A relatively small fraction of ADV measurements have been made from moorings (e.g., Fer
⁴³ and Paskyabi 2014). Presumably this is because mooring motion can contaminate ADV mea-
⁴⁴ surements, and acoustic Doppler profilers (ADPs) can be used to measure mid-depth turbulence
⁴⁵ statistics without a mooring (e.g., Stacey et al. 1999a; Rippeth et al. 2002; Wiles et al. 2006).
⁴⁶ Still, ADV measurements have distinct characteristics that can be advantageous: they are capa-
⁴⁷ ble of higher sample rates, have higher signal-to-noise ratios, and have a much smaller sample
⁴⁸ volume (1 centimeter, as opposed to several meters). That is, compared to an ADP, ADVs are
⁴⁹ high-precision instruments capable of providing unique information. They could be more widely
⁵⁰ used as a moored instrument (i.e., at an arbitrary depth) if a method for accounting for mooring
⁵¹ motion can be demonstrated to provide more accurate estimates of turbulence statistics.

⁵² Inertial motion unit (IMU) sensors have been used in the aerospace and aeronautical industries
⁵³ to quantify the motion of a wide range of systems, and to improve atmospheric velocity measure-
⁵⁴ ments, for several decades (Axford 1968; Edson et al. 1998; Bevly 2004). Over the last 10 years,
⁵⁵ the smartphone, drone, and ‘Internet of Things’ markets have driven innovation in microelectrical-
⁵⁶ mechanical systems, including the IMU. As a result of this growth and innovation, the cost, power

57 requirements, and size of IMUs have come down. These changes have allowed these sensors to be
58 integrated into oceanographic instruments that have small form-factors, and rely on battery power.
59 Nortek now offers a version of their Vector ADV with a Microstrain 3DM-GX3-25 IMU sensor
60 (Nortek 2005; MicroStrain 2012). This IMU's signals are incorporated into the Vector data stream,
61 so that its motion and orientation signals are tightly synchronized with the ADV's velocity mea-
62 surements. This tight synchronization provides a data stream that can be utilized to quantify ADV
63 motion in the Earth's inertial reference frame, and remove that motion from the ADV's velocity
64 measurements at each time step of its sampling (Edson et al. 1998). This work utilizes moored
65 'ADV-IMU' measurements from mid-depths in Puget Sound to demonstrate that motion correc-
66 tion can improve the accuracy of oceanic turbulence spectra, turbulence dissipation, and Reynolds
67 stress estimates from moored platforms.

68 This effort was originally motivated by a need for low-cost, high-precision turbulence measure-
69 ments for the emerging tidal energy industry (McCaffrey et al. 2015; Alexander and Hamlington
70 2015). Experience in the wind energy industry has shown that wind turbine lifetime is reduced
71 by atmospheric turbulence, and the same is expected to be true for tidal energy turbines. In the
72 atmosphere, meteorological towers are often used to position sonic anemometers at the hub height
73 of wind turbines for measuring detailed turbulence inflow statistics (Hand et al. 2003; Kelley et al.
74 2005; Mücke et al. 2011; Afgan et al. 2013). In the ocean, tower-mounted hub-height turbulence
75 measurements have been made, but they are challenging to install and maintain in energetic tidal
76 sites (Gunawan et al. 2014; Thomson et al. 2012). Therefore, the U.S. Department of Energy
77 funded this work to investigate the accuracy of mooring-deployed ADV-IMUs to reduce the cost
78 of turbulence measurements at tidal energy sites (Kilcher et al. 2016). The approach proved to be
79 successful and potentially useful to the broader oceanographic community interested in moored

80 turbulence measurements (Lueck and Huang 1999; Doherty et al. 1999; Nash et al. 2004; Perlin
81 and Moum 2012; Alford 2010; Paskyabi and Fer 2013).

82 The next section describes details of the measurements, including a summary of the hardware
83 configurations (platforms) that were used to support and position the ADV-IMUs in the water
84 column. A detailed description of the motion of these platforms is found in the companion paper to
85 this work, Harding et al. (in review), hereafter Part 1. Section 3 describes the mathematical details
86 of motion correction and Section 4 presents results from applying the method to measurements
87 from the various platforms. Section 5 is a discussion of the energetics of the tidal channel in
88 which the measurements were made and demonstrates that the measurements are consistent with
89 turbulence theory and other measurements in similar regimes. A summary and concluding remarks
90 are provided in Section 6.

91 **2. Measurements**

92 This work focuses on measuring turbulence from ADVs that are equipped with IMUs and de-
93 ployed from moving (moored) platforms. The ADVs utilized for these measurements were Nortek
94 Vector ADVs equipped with Microstrain 3DM-GX3-25 IMU sensors. These IMUs captured all
95 six components of the ADV motion (three components of angular rotation and three components
96 of linear acceleration), as well as the orientation of the ADV pressure case. The sampling of the
97 motion sensor is tightly synchronized with the ADV measurements. The IMU measures its mo-
98 tion at 1 kHz and uses internal signal integration (Kalman filtering) to output the motion signals
99 at the same sample rate as the ADV's velocity measurements. This reduces aliasing of the IMU's
100 motion measurements above the ADV's sample rate (MicroStrain 2010). Cable-head ADVs were
101 used throughout this work to allow for flexibility in the positioning of the ADV head relative to its
102 pressure case.

103 All measurements used in this work were made in Admiralty Inlet, Washington, approximately
104 500 m west southwest of Admiralty Head in 60 m of water near 48° 9.18' N, 122° 41.22' W (Figure
105 1). The site is approximately 6 km east of Port Townsend, and 1 km north of the Port Townsend
106 to Coupeville ferry route. Admiralty inlet is the largest waterway connecting Puget Sound to
107 the Strait of Juan de Fuca, and it possesses a large semidiurnal tidal flow (Thomson et al. 2012;
108 Polagye and Thomson 2013). This work utilizes data from three distinct deployment platforms:
109 the tidal turbulence mooring, a StableMoor buoy, and a simple sounding weight. All data used
110 in this analysis are available from the MHK data repository (<http://mhkdr.openei.org>; submission
111 ids: 49, 50 and 51). Each of these platforms are briefly described below, and additional details,
112 photos, and schematic diagrams can be found in Part 1.

113 *a. Tidal Turbulence Mooring*

114 The tidal turbulence mooring (TTM) is a simple mooring system with a strongback fin sus-
115 pended between a steel clump-weight anchor weighing 1,200 kg when dry and a 0.93-m-diameter
116 spherical steel buoy with a buoyancy of 320 kg. The ADV pressure cases were clamped to one
117 side of the strongback fin and the ADV sensor head was positioned 10 cm in front of the fin's
118 leading edge (Figure 2). The leading edge of the fin is fastened inline with the mooring line. This
119 configuration was designed to work like a weather vane, such that the drag on the fin held the ADV
120 head upstream of the mooring components. This work utilizes data from two TTM deployments.

121 The first TTM deployment was in June 2012 from 17:30 on the 12th until 14:30 on the 14th
122 (local; i.e., Pacific Daylight Time). Two Nortek ADVs were clamped to either side of the fin so that
123 the axis of their cylindrical pressure cases were parallel with the leading edge of the strongback.
124 The ADV heads were spaced 0.5 m apart vertically along the fin. Only one of these ADVs was

¹²⁵ equipped with an integrated IMU. This TTM also had an upward-looking acoustic Doppler profiler
¹²⁶ mounted on the mooring anchor.

¹²⁷ Periods of time during which this mooring interfered with a beam of the Doppler profiler were
¹²⁸ identified by inspecting the profiler's acoustic amplitude signal. Periods during which one beam
¹²⁹ of the profiler had $> 5\%$ higher acoustic amplitude than the other beams were flagged as "contam-
¹³⁰ inated" and excluded from averaging. Five-minute averages in which more than 50% of the data
¹³¹ were contaminated in this way were masked as invalid.

¹³² The second TTM deployment was in 2014 from 06:00 on June 17 to 05:00 on June 19 (local
¹³³ time). Two Nortek ADV-IMUs were mounted on this TTM, with their heads spaced 0.5 m apart
¹³⁴ along the fin. In this case, the pressure cases and ADV heads were inclined at an angle of 18° to
¹³⁵ the leading edge of the fin to account for mooring blowdown during strong currents (Figure 3).
¹³⁶ This change was made to reduce vibrational motion observed during the June 2012 deployment
¹³⁷ that was believed to be associated with the orientation of the pressure cases.

¹³⁸ *b. The StableMoor platform*

¹³⁹ The second deployment platform was a cylindrical, StableMoor, syntactic foam buoy (manufac-
¹⁴⁰ turer: Deep Water Buoyancy) that was anchored to a clump weight that weighed 1,200 kg (Figure
¹⁴¹ 4). The buoy is 3.5 m long and 0.45 m in diameter with a tail ring that is 0.76 m in diameter. The
¹⁴² StableMoor buoy weighs 295 kg in air, and has a buoyancy of 185 kg in water.

¹⁴³ The StableMoor buoy was deployed with an ADV-IMU mounted at its nose from 11:21 on May
¹⁴⁴ 12 to 11:53 on May 13, 2015 (local time). The sample volume of the ADV is 10 cm forward of
¹⁴⁵ the nose and 20 cm above the center line of the StableMoor buoy (Figure 4). Based on Wyngaard
¹⁴⁶ et al.'s (1985) investigation of a similarly shaped slender body, the velocity measurements should
¹⁴⁷ have flow-distortion effects of less than 10%. This configuration was designed to be the most

¹⁴⁸ stable platform for measuring turbulence from a moving platform. The StableMoor buoy was
¹⁴⁹ equipped with a 1,200-kHz RDI workhorse sentinel acoustic Doppler profiler that was oriented
¹⁵⁰ downward-looking to measure water velocity below the platform in twelve 1-m bins and measure
¹⁵¹ buoy motion (“bottom tracking”), all at a 1-Hz sample rate.

¹⁵² The buoy was ballasted to pitch upward a few degrees in zero-flow to avoid “flying downward”.
¹⁵³ In the presence of an oncoming current, the tail fins help to orient it into the flow. The anchor for
¹⁵⁴ this buoy is similar to that of the TTM, including an acoustic release so the mooring and anchor
¹⁵⁵ can be recovered separately.

¹⁵⁶ The StableMoor platform has two primary advantages compared to the TTM. First, it is signif-
¹⁵⁷ icantly more massive and hydrodynamically stable than the TTM, which reduces the frequency
¹⁵⁸ of motions of the platform. Second, the StableMoor platform is capable of supporting a bottom-
¹⁵⁹ tracking acoustic Doppler profiler, which provides an independent measure of the platform’s trans-
¹⁶⁰ lational motion. Disadvantages of the StableMoor include: its size, which adds to the challenge of
¹⁶¹ deployment and recovery, and its cost, which is significantly higher than the TTM system.

¹⁶² *c. Turbulence Torpedo*

¹⁶³ The turbulence torpedo is a simple sounding weight with an ADV head mounted forward of the
¹⁶⁴ nose, and the ADV pressure case strapped below (Figure 5). This platform was deployed on May
¹⁶⁵ 14, 2015, for 37 minutes starting at 07:41 local time. This measurement was made from a davit
¹⁶⁶ that hung the system from the side of the ship to a depth of approximately 25 m. The primary
¹⁶⁷ logistical advantages of this platform are its compact size, low cost, and the flexibility to perform
¹⁶⁸ spatial transects.

¹⁶⁹ *d. Coordinate system and turbulence averaging*

¹⁷⁰ Unless stated otherwise, vector quantities in this work are in a fixed “principal-axes” coordinate
¹⁷¹ system that is aligned with the bidirectional tidal flow: positive u is in the direction of ebb (310°
¹⁷² True), positive w is vertically upward, and v is the cross-stream component in a right-handed
¹⁷³ coordinate system. The full velocity vector, $\vec{\tilde{u}} = (\tilde{u}, \tilde{v}, \tilde{w})$, is separated into a mean and turbulent
¹⁷⁴ component as $\vec{\tilde{u}} = \vec{\bar{u}} + \vec{u}$, where the over-bar denotes a 5-minute average. Turbulence kinetic
¹⁷⁵ energy, $\text{tke} = \overline{u^2} + \overline{v^2} + \overline{w^2}$, and Reynold’s stresses, \overline{uv} , \overline{uw} , \overline{vw} , are computed by averaging over the
¹⁷⁶ 5-minute window. Throughout this work, we use $\bar{U} = (\bar{u}^2 + \bar{v}^2)^{1/2}$ to denote the mean horizontal
¹⁷⁷ velocity magnitude.

¹⁷⁸ All spectra, $S\{x\}(f) = |\mathcal{F}\{x(t)\}|^2$, and cross spectra, $C\{x,y\}(f) = \text{real}(\mathcal{F}\{x(t)\}\mathcal{F}\{y(t)\})$, are
¹⁷⁹ computed using NumPy fast Fourier transform routines (van der Walt et al. 2011). Here, $\mathcal{F}\{x(t)\}$
¹⁸⁰ denotes the fast Fourier transform of a signal $x(t)$. Time series, e.g., $x(t)$, are linearly detrended
¹⁸¹ and Hanning windowed prior to computing $\mathcal{F}\{x\}$ to reduce spectral reddening.

¹⁸² Throughout the remainder of this work, the dependence of S and C on f is implied (e.g., $S\{x\}(f)$
¹⁸³ is hereafter $S\{x\}$), and for other variables the dependence on t is implied. Spectra and cross spectra
¹⁸⁴ are normalized to preserve variance; e.g., $\int S\{u\}df = \overline{u^2}$, and $\int C\{u,v\}df = \overline{uv}$. The notations
¹⁸⁵ $S\{\vec{u}\} = (S\{u\}, S\{v\}, S\{w\})$, and $C\{\vec{u}\} = (C\{u,v\}, C\{u,w\}, C\{v,w\})$ denote the set of spectra and
¹⁸⁶ cross spectra for each velocity component and pairs of components, respectively.

¹⁸⁷ Turbulence dissipation rates are computed as:

$$\epsilon = \frac{1}{\bar{U}} \left(\alpha \left\langle (S\{u\} + S\{v\} + S\{w\}) f^{5/3} \right\rangle_{f_{IS}} \right)^{3/2} \quad (1)$$

¹⁸⁸ where $\alpha = 0.5$ and $\langle \rangle_{f_{IS}}$ denotes an average over the inertial subrange of the velocity spectra and
¹⁸⁹ where the signal-to-noise ratio is small (Lumley and Terray 1983; Sreenivasan 1995). Throughout

190 this work, we take this average from 0.3 to 1 Hz for the u and v components, and 0.3 to 3 Hz for
 191 the w component.

192 3. Methodology

193 This work describes a method for correcting velocity measurements from a moving velocity
 194 sensor, \vec{u}_m , using independent measurements of that sensor's motion, \vec{u}_h , to remove the motion
 195 from the velocity measurements, and thus estimate the 'motion corrected velocity':

$$\vec{u}(t) = \vec{u}_m(t) + \vec{u}_h(t) \quad . \quad (2)$$

196 Note here that the '+'-sign is correct because head motion, \vec{u}_h , induces a measured velocity in
 197 the opposite direction of the head motion itself ($\vec{u}_m = \vec{u} - \vec{u}_h$). This approach has been used
 198 to successfully correct sonic anemometer measurements of atmospheric turbulence (e.g., Edson
 199 et al. 1998; Miller et al. 2008). In the ocean, previous works have utilized inertial motion sensors
 200 to quantify the motion of multiscale profilers for the purpose of measuring the full spectrum of
 201 oceanic shear (Winkel et al. 1996), and to quantify the motion of thermistor sensors (Moum and
 202 Nash 2009), but the Edson et al. (1998) approach has not been documented for moored ADV
 203 measurements.

204 The Microstrain IMU available in the Nortek Vector ADV measures the linear acceleration, \vec{a} ,
 205 rotational motion, $\vec{\omega}$, and orientation matrix, \mathbf{R} , of the ADV pressure case in the Earth reference
 206 frame at every time step of the ADV's sampling. So long as the ADV head is rigidly connected
 207 to the IMU (i.e. the ADV pressure case), the motion of the ADV head is calculated from these
 208 signals as the sum of rotational and translational motion:

$$\begin{aligned} \vec{u}_h &= \vec{u}_\omega + \vec{u}_a + \vec{u}_{\text{low}} \\ &= \mathbf{R}^T \cdot \vec{\omega}^*(t) \times \vec{l}^* + \int \{\vec{a}(t)\}_{HP(f_a)} dt + \vec{u}_{\text{low}} \end{aligned} \quad (3)$$

209 Here, $*$ superscripts denote quantities in the ADV’s local coordinate system, and $\vec{\ell}^*$ is the vec-
 210 tor from the IMU to the ADV head. \mathbf{R}^T —the inverse of the orientation matrix—rotates vectors
 211 from the IMU to the Earth reference frame. The notation $\{\vec{a}\}_{HP(f_a)}$ indicates that the IMU’s ac-
 212 celerometer signal is high-pass filtered (in the Earth’s stationary reference frame) at a chosen filter
 213 frequency, f_a . Without such filtering, low-frequency noise in \vec{a} —sometimes referred to as bias
 214 drift—is amplified by integration to the point that it overwhelms the higher frequency information
 215 (Barshan and Durrant-Whyte 1995; Bevly 2004; Gulmammadov 2009). $\vec{\tilde{u}}_{\text{low}}$ is the low-frequency
 216 translational motion that is unresolved by \vec{u}_a , and it is discussed in more detail below. Note that,
 217 to avoid double counting, $\vec{\tilde{u}}_{\text{low}}$ should be estimated by applying the complementary low-pass fil-
 218 ter to the independent measurement of low-frequency motion. We use fourth order, zero-phase
 219 (bidirectional), Hanning filters for all filtering operations.

220 The noise levels of the IMU, \vec{n}_ω and \vec{n}_a , are computed from ADV-IMU data collected while the
 221 instrument was resting motionless on a table for several hours. Where, for this motionless dataset,
 222 the noise levels are defined according to (3) with \vec{n}_ω in place of $\vec{\tilde{u}}_\omega$, and \vec{n}_a in place of $\vec{\tilde{u}}_a$. These
 223 are presented in Figure 6 relative to the ADV spectra presented in following sections of this paper
 224 (grey shading), and relative to the Doppler noise levels of the ADV.

225 $S\{\vec{n}_\omega\}$ is equal in all three components, and so only one component is presented for simplicity
 226 (yellow). $S\{\vec{n}_\omega\}$ is several orders of magnitude lower than the velocity spectra we measured
 227 (grey region), and also more than an order of magnitude smaller than the Doppler noise levels of
 228 the ADV. Here we have used $\vec{\ell}^* = 1$ m; which is the order-of-magnitude of the typical distance
 229 between the ADV head and the IMU. This indicates that the precision of $\vec{\tilde{u}}_\omega$ (i.e. the angular rate
 230 sensor) is adequate for making corrections to ADV velocity measurements without filtering.

231 The noise level of $S\{\vec{\tilde{u}}_a\}$ (Figure 6, black), on the other hand, is dominated by a f^{-2} slope
 232 that results from integrating the low-frequency noise in \vec{a} . The horizontal (u and v) spectra of

these noise levels are identical, and so we only present one of them for simplicity (solid lines).
The vertical spectra noise levels are different because the signal-to-noise ratio is larger (dashed
black lines). High-pass filtering reduces the low-frequency noise (purple and green) so that it does
not contaminate motion correction, but any real motion that does exist at these frequencies is lost
(Egeland 2014; VanZwieten et al. 2015). This means there is a residual low-frequency translational
motion, \vec{u}_{low} , that needs to be measured independently—or at the very least considered—when
using ADV-IMU data from moving platforms.

For the StableMoor buoy, the ADP bottom-track measured \vec{u}_{low} , and this measurement agrees
with \vec{u}_a over a narrow frequency band (see Part I, appendix A), indicating that the ADP and IMU
are resolving the same motion. When this is the case, it is trivial to select a frequency in the
middle of the spectral overlap (in this case, we choose $f_a = 0.2$ Hz), and high-pass and low-
pass filter \vec{u}_a and \vec{u}_{low} , respectively, then sum to estimate total translational motion. This process
gives a noteworthy improvement in the shape of $S\{u\}$ and $S\{v\}$ for the StableMoor buoy when
compared to assuming $\vec{u}_{\text{low}} = 0$ (not shown). This indicates that ADP bottom-track measurements
are important for resolving turbulence spectra from the StableMoor buoy platform.

The position of the TTM ADV can be estimated, relative to its base, by assuming the moor-
ing acts like a rigid pole and using the IMU orientation matrix to estimate the pole’s ‘lean’. The
position obtained from this model can then be differentiated to estimate \vec{u}_{low} (this model does
not apply at high frequencies). Spectra of \vec{u}_{low} estimated using this approach for the June 2014
TTM deployment (Figure 6, blue) are plotted up to the point where they cross their respective
 $S\{\vec{u}_a\}$ noise level (black). Together, these two lines provide an ‘aggregate noise level’ of transla-
tional velocity estimates for the TTM: the rigid pole estimate of \vec{u}_{low} indicates the amplitude of
unresolved motion at low- f (blue), and $S\{\vec{u}_a\}$ indicates the limits of the IMU at high- f (black).
Coincidentally, $S\{\vec{u}_a\}$ filtered at $f_a = 0.0333\text{Hz}$ is not a terrible approximation for this aggregate

noise level. Furthermore, because this aggregate noise level is more than an order of magnitude lower than the velocity spectra of interest (shaded region), the results of motion correction are essentially identical whether we use the rigid pole model to estimate \vec{u}_{low} , or if we simply assume that $\vec{u}_{\text{low}} = 0$.

The choice of f_a does influence the effectiveness of motion correction (Figure 7). When f_a is too high (e.g., 0.33 Hz, red), the high-pass filter removes resolved motion from \vec{u}_h that could be used to correct velocity measurements. In particular, notice that the amplitude of the 0.15 Hz peak—which is clearly the result of motion contamination (grey line)—is reduced significantly when we preserve more \vec{u}_h information by reducing the high pass filter frequency to $f_a = 0.033$ Hz. Further reducing f_a to 0.0033 Hz does not reduce the peak further, but does increase the amplitude of the spectra at low-frequency. This low- f increase is the IMU-accelerometer’s low-frequency bias drift (Figure 6) returning to contaminate the motion correction method.

Based on the above, we conclude that $f_a = 0.033$ Hz is a convenient ‘middle’ frequency that reduces accelerometer bias-drift without destroying resolved motion of the TTM. The same $f_a = 0.033$ Hz filter was selected, based on a similar analysis, for the turbulence torpedo. The reader is likely to notice that the 0.15 Hz peak is not completely removed by motion correction, especially for the v component (Figure 7, middle panel). We will discuss this ‘persistent motion contamination’ further in the following section.

Thus, we find that filter selection involves a trade-off between filtering out the bias drift noise at low-frequencies while not filtering out measured motion at high frequencies. In general, this will depend on the dynamics of the platform used to support the ADV, and the intensity of the turbulence being measured. When an independent measurement of \vec{u}_{low} is available the cross-coherence with \vec{u}_a can indicate a region of spectral overlap, and f_a can be selected at the midpoint.

280 Lacking a reliable estimate of \vec{u}_{low} , the value of f_a that produces the lowest tke estimates is likely
281 the best.

282 Additional details on motion correction—including a detailed accounting of the distinct co-
283 ordinate systems of the IMU, ADV pressure case, and ADV head—can be found in Kilcher
284 et al. (2016). Open-source Python tools for performing motion correction of ADV-IMU data—
285 including scripts that write processed data in Matlab and tabulated formats—are available at
286 <http://lkilcher.github.io/dolfyn/>.

287 4. Results

288 a. Mean velocity

289 Figure 8 shows a comparison of \vec{u} measured by an ADV-IMU mounted on a TTM, to an upward-
290 looking acoustic Doppler profiler mounted on the TTM anchor. This comparison shows excellent
291 agreement between the ADV and Doppler profiler measurements of mean velocity. The \bar{u} , \bar{v} , and
292 \bar{w} components have a root-mean-square error of 0.05, 0.13, and 0.03 m/s, respectively. Although
293 it is important to note that there is some discrepancy between ADP- and ADV-measured velocities
294 (especially in \bar{v} , which is most likely due to incomplete motion correction), the agreement between
295 the magnitude and direction of these independent velocity measurements indicates that moored
296 ADV-IMUs provide a reliable estimate of mean velocity in the Earth’s reference frame.

297 b. TTM spectra

298 As discussed in detail in Part 1, the mooring motion of the TTM, $S\{\vec{u}_h\}$, has a peak at 0.1 to 0.2
299 Hz from swaying of the mooring that is most likely driven by eddy shedding from the spherical
300 buoy (Figure 9, red lines). There is also higher-frequency broadband motion that is associated
301 with fluttering of the strongback fin around the mooring line. Both of these motions are especially

302 energetic in the v -component spectra because this is the direction in which the TTM mooring
303 system is most unstable. As is expected from fluid-structure interaction theory, the amplitude of
304 these motions increases with increasing mean velocity (Morison et al. 1950).

305 The mooring motion contaminates the uncorrected ADV measurements of velocity, $S\{\vec{u}_m\}$,
306 whenever the amplitude of the motion is similar to or greater than the amplitude of the turbu-
307 lence. Fortunately, much of this motion can be removed using the IMU's motion signals as de-
308 tailed in Section 3. Lacking an independent measurement of turbulence velocity at this site, we
309 interpret the agreement of these spectra with turbulence theory as evidence that motion correc-
310 tion has improved the velocity measurements. In particular, at high frequencies ($f > 0.3$ Hz) for
311 each mean-flow speed, the spectra decay with a $f^{-5/3}$ slope and have equal amplitude across the
312 velocity components. These results are consistent with Kolmogorov's (1941) theory of isotropic
313 turbulence, and are consistent with spectral shapes of earlier measurements of turbulence in ener-
314 getic tidal channels from stationary platforms (Walter et al. 2011; Thomson et al. 2012; McMillan
315 et al. 2016).

316 For $|\vec{u}| > 1.0$, motion correction modifies the u and v component spectra at frequencies as high
317 as 3 Hz. This outcome indicates that in order for motion correction to be effective, synchronization
318 between the ADV and IMU needs to be within 1/3 s or better. This suggests that asynchronous
319 approaches to motion correction may be challenging, especially considering that the clock drift of
320 some instrumentation can be as high as a few seconds per day. By integrating the IMU data into
321 the ADV data stream, the Nortek ADV-IMU achieves a synchronization to within 1e-2 s.

322 At low frequencies the spectra tend to become roughly constant (especially at higher flow
323 speeds), which is also consistent with previous works. Note that the very low magnitude of $S\{\vec{u}_h\}$
324 at low frequencies is partially a result of filtering the IMU's accelerometer signal when calculating
325 \vec{u}_a . The true low-frequency spectrum of ADV head motion is unknown (indicated using a dashed

326 line below f_a). A comparison of $S\{\vec{u}\}$ measured by the TTM to that measured by the ADP—during
327 the June 2012 deployment—reveals agreement at low frequencies (not shown). This finding sug-
328 gests that the assumption that $\vec{u}_{\text{low}} = 0$ at these frequencies and at this site for this platform is
329 justified—even if $S\{\vec{u}_h\}$ is not as low as indicated in Figure 9.

330 As successful as motion correction is, some of the motion contamination persists in $S\{\vec{u}\}$. This
331 is most notable in $S\{v\}$ at the highest flow speeds (> 2.0 m/s): a peak at 0.15 Hz is an order of
332 magnitude larger than a spectral fit to the other frequencies would indicate. This persistent motion
333 contamination is evident to a lesser degree in $S\{u\}$ for $|u| > 2$ m/s, and in $S\{v\}$ at lower flow
334 speeds. $S\{w\}$ appears to have no persistent motion contamination because the amplitude of the
335 motion in this direction is much lower than for the other two components. For these measurements,
336 $S\{w_h\}$ is so low that w -component motion correction makes only a minor correction to the spectra.

337 The amplitude of the persistent motion contamination peaks in $S\{v\}$ at 0.15 Hz is a factor of 5
338 to 10 times smaller than the amplitude of the ADV head motion itself. This observation suggests
339 that the Microstrain IMU can be used to effectively correct mooring motion at 0.15 Hz when
340 the amplitude of that motion is less than 5 times the amplitude of the real turbulence spectrum.
341 As a result, we have chosen a value of 3 as a conservative estimate of the motion correction's
342 effectiveness.

343 In addition to the primary benefit of correcting for mooring motion, the IMU measurements
344 can also be used to identify and screen out persistent motion contamination. For example, one
345 of the most common uses of turbulence spectra is for the calculation of ϵ and tke. For these
346 purposes, and based on the relative amplitudes of the 0.15-Hz peaks, we assume that persistent
347 motion contamination is likely, where $S\{\vec{u}_h\}/S\{\vec{u}\} > 3$, and thereby exclude these regions from
348 spectral fits.

349 In the present case, for the u and w spectra, this criteria only excludes a narrow range of frequen-
350 cies at the 0.15-Hz motion peak for some cases. This criteria is more restrictive of the v -component
351 spectra at high frequencies for $\bar{U} > 1.0$ m/s, but this may be acceptable because the amplitude of
352 $S\{v\}$ at these frequencies—i.e., in the isotropic inertial subrange—should be equal to that of $S\{u\}$
353 and $S\{w\}$ (Kolmogorov 1941).

354 Agreement of the v -component spectral amplitude with that of u and w at frequencies > 0.3 Hz
355 indicates that motion correction is effective at those frequencies even when $S\{\vec{u}_h\}/S\{\vec{u}\} \gtrsim 3$. This
356 outcome suggests that our screening threshold is excessively conservative at those frequencies,
357 and that a more precise screening threshold may be frequency dependent. For example, it might
358 take into account the f^3 character of the noise in $S\{\vec{u}_a\}$ (Figure 6). For the purpose of this work,
359 the $S\{\vec{u}_h\}/S\{\vec{u}\} < 3$ threshold for spectral fits is sufficient, and detailed characterization of the
360 IMU’s motion- and frequency-dependent noise level is left for future work.

361 *c. StableMoor Spectra*

362 The spectra of the StableMoor motion has a broader peak with a maximum amplitude that is ap-
363 proximately half the frequency of the TTM spectral peak (Figure 10). The motion of this platform
364 also does not have high-frequency “subpeaks” or other high-frequency broadband excitation
365 (Part 1). These characteristics of the motion are most likely due to the more massive and hydro-
366 dynamically streamlined properties of the platform.

367 Like the TTM, the motion-corrected spectra from the StableMoor buoy are consistent with turbu-
368 lence theory and previous observations. Most importantly, there is an improvement in the quality
369 of the motion-corrected spectra compared to the TTM. In particular, the persistent motion con-
370 tamination peaks are completely removed. That is, this measurement system provides an accurate

371 estimate of the turbulence spectra at this location from low frequencies to more than 1 Hz—well
372 into the inertial subrange—for all three components of velocity.

373 Note that this level of accuracy cannot be obtained without the independent estimate of \vec{u}_{low} .
374 If we assume that $\vec{u}_{\text{low}} = 0$, a similar plot to Figure 10 (not shown) reveals persistent motion-
375 contamination peaks and troughs in the u and v spectra regardless of the choice of f_a . This as-
376 sumption indicates that the low-frequency motion of the StableMoor buoy is below a threshold in
377 which the IMU’s signal-to-noise ratio is high enough to resolve its motion. In other words, com-
378 pared to the TTM, the StableMoor platform provides a more accurate measurement of turbulence
379 when it includes an independent measure of \vec{u}_{low} (here a bottom-tracking ADCP), but it does no
380 better—and perhaps worse—when it does not.

381 *d. Torpedo spectra*

382 The u and v motion of the turbulence torpedo is broadband and the w motion has a narrow peak
383 at 0.3 Hz (Figure 11). Because \vec{u}_h is estimated using $f_a = 0.0333 \text{ Hz}$ and assuming $\vec{u}_{\text{low}} = 0$, its
384 spectra rolls off quickly below f_a . Motion correction of the torpedo data appears to effectively re-
385 move a motion peak from $S\{w\}$ at 0.3 Hz, and straightens out $S\{v\}$ between 0.04 and 0.6 Hz. $S\{u\}$
386 is mostly unaffected by motion at these frequencies, because the torpedo motion is smaller than
387 the turbulence in this direction. At frequencies below f_a , $S\{u\}$ and $S\{v\}$ increase dramatically.
388 This increase suggests that unresolved, low-frequency motion of the torpedo is contaminating the
389 velocity measurements at these frequencies. It may be possible to correct for some of this con-
390 tamination using a measurement of the ship’s motion as a proxy for the torpedo’s low-frequency
391 motion, but this has not been done. Still, above f_a , the torpedo appears to provide a reliable
392 estimate of spectral amplitude in the inertial subrange and can therefore be used to estimate ε .
393 Considering the simplicity of the platform, it may be a useful option for quantifying this turbu-

394 lence statistic in a variety of scenarios. Further, if a GPS is positioned above it, it may be capable
395 of providing even more.

396 *e. Cross Spectra*

397 Cross-spectra indicate the correlation between different velocity components as a function of
398 frequency, and their integrals are the Reynold's stresses. Head motion cross-spectra, $C\{\vec{u}_h\}$ (Figure
399 12, red), and uncorrected velocity cross-spectra, $C\{\vec{u}_m\}$ (black), from TTM measurements have
400 large peaks at the same frequency (0.15 Hz) as peaks in auto-spectra (Figure 9). This indicates
401 that mooring motion contaminates the uncorrected cross-spectral velocity measurements, and that
402 Reynold's stress estimates based on uncorrected velocity measurements will be contaminated by
403 mooring motion. This makes sense because mooring swaying in a direction not aligned with one
404 of the major principal axes will, for example, introduce spurious cross-spectra and contaminate
405 the Reynold's stress.

406 Fortunately, motion corrected velocity cross-spectra, $C\{\vec{u}\}$ (blue), have reduced spectral ampli-
407 tudes at these frequencies (reduced peaks), which indicates that motion correction reduces motion
408 contamination to produce more reliable estimates of velocity cross spectra and Reynold's stresses
409 (Figure 12). In particular, the uncertainty in $f \cdot C\{\vec{u}\}$ (indicated by the blue shading), is signifi-
410 cantly smaller than the mean values of $C\{\vec{u}_h\}$ and $C\{\vec{u}_m\}$ at the frequencies of maximum motion
411 (0.15 Hz). This indicates that even the individual estimates of $C\{\vec{u}\}$ have reduced peaks at these
412 frequencies, not just the mean.

413 These results indicate that motion-corrected TTM velocity measurements can be used to obtain
414 reliable estimates of turbulence Reynold's stresses, which are the integral of the cross spectra.
415 Without motion correction, Reynold's stress estimates would be contaminated by the large peaks
416 in the cross spectra that are caused by the swaying and fluttering motion of the TTM vane.

417 A similar investigation of StableMoor cross spectra (not shown) indicates that cross-spectral
418 motion contamination is at a much lower amplitude than for the TTM. The low-frequency (< 0.3
419 Hz) “swimming” motion of that platform produces a minimal cross-spectral signal, and the relative
420 large mass of the platform minimizes the kinds of higher-frequency swaying and fluttering that
421 creates large values of cross-spectral head motion. Thus, the StableMoor platform also produces
422 reliable estimates of Reynold’s stresses, which are presumed to be improved by motion correction.

423 5. Discussion

424 The previous section presented a comparison of \vec{u} measured by a TTM-mounted ADV to mea-
425 surements from a co-located ADP. This comparison demonstrated that the IMU provides a reliable
426 estimate of the ADV’s orientation and that this can be utilized to estimate mean velocity in the
427 Earth’s reference frame. Turbulence velocity estimates from the same ADP are also in agree-
428 ment with low-frequency TTM turbulence estimates (not shown), but the ADP does not resolve
429 turbulence at the scales where motion contamination is strongest (0.1 to 1.0 Hz).

430 Ideally, moored motion-corrected turbulence velocity measurements would be validated against
431 simultaneous independent validated measurements of turbulence velocity at the same scales and
432 exact time and location. Accomplishing this, however, involves significant technical challenges
433 that are not easily overcome—most notably the difficulty of measuring turbulence at the same point
434 as the moving ADV. A slightly less ideal but much more realistic confirmation of the methodology
435 might involve comparing the statistics of moored turbulence measurements to those from a nearby
436 fixed platform, or a fixed platform placed at the same location at a different time (e.g., the “TTT”
437 platform described in Thomson et al. 2012). Unfortunately, to our knowledge, these measurements
438 have not yet been made.

439 Lacking a relevant, fixed, independent turbulence measurement to compare to it is instructive
 440 to demonstrate the degree to which the moored measurements are consistent with turbulence
 441 theory and other turbulence measurements in similar flow environments. The previous section
 442 showed that the shape of the turbulence velocity spectra from moored ADVs is consistent with
 443 Kolmogorov's theory of locally isotropic turbulence, which has been observed consistently in tur-
 444 bulence measurements for decades (Kolmogorov 1941; Grant et al. 1962; McMillan et al. 2016).
 445 In particular, we observed an isotropic subrange—an $f^{-5/3}$ spectral slope and equal amplitude
 446 spectra between components—that is driven by anisotropic turbulence at longer timescales (Fig-
 447 ures 9, 10, 11). This finding is interpreted as the first indication that the measurement systems
 448 presented are capable of accurately resolving turbulence. The degree to which uncorrected spec-
 449 tra were corrected toward this theoretical and observationally confirmed shape is interpreted as a
 450 measure of the improvement of the spectral estimates by motion correction.

451 Figure 13 presents a time series of the mean velocity (A) and several turbulence statistics that
 452 were measured during the June 2014 TTM deployment. This figure shows the evolution of the flow
 453 through Admiralty Inlet during 1.5 tidal cycles. The tke (B), Reynold's stresses (C), dissipation,
 454 and one component of turbulence production (D) grow and strengthen with ebb or flood then
 455 subside during slack tide. This component of turbulence production is:

$$P_{uz} = \bar{uw} \frac{\partial \bar{u}}{\partial z} . \quad (4)$$

456 Where $\partial \bar{u} / \partial z$ is computed from the two ADVs on the TTM. The highest values of ε and P_{uz} occur
 457 at the peak of the ebb or flood, which is in agreement with other measurements in tidal channels.
 458 The agreement of the magnitude of P_{uz} with ε at those times suggests a local production-dissipation
 459 balance that is often observed in tidally forced channels (Trowbridge et al. 1999; Stacey et al.

460 1999b; McMillan et al. 2016). At other times, the value of P_{uz} is insufficient to balance ε or is
461 negative.

462 Inspection of the negative P_{uz} values reveals that most of them are caused by a reversed sign of \bar{uw}
463 rather than a reversed sign of $\partial u / \partial z$ (i.e., when compared to the sign of u). This finding suggests
464 that uncertainty in \bar{uw} may be contributing to discrepancies between P_{uz} and ε . Furthermore,
465 considering the complex nature of the bathymetry and shoreline at this site (i.e., the headland), it
466 is not surprising that P_{uz} does not perfectly balance ε . Other terms of the tke equation are likely
467 to be important, such as turbulence advection, other components of production, and turbulent
468 transport. The fact that the P_{uz} and ε terms are in near balance as often as they are indicates that
469 bottom boundary layer physics are important to the turbulence dynamics at this site.

470 Figure 14 compares individual values of P_{uz} with ε directly. Given the assumptions implicit in
471 this comparison and the discussion above, the degree of agreement between P_{uz} and ε —especially
472 for the highest values of ε —suggests the turbulent boundary layer reaches the depth of these mea-
473 surements (10 m) during the highest flow speeds. This result is further supported by a comparison
474 of \bar{U} with ε (Figure 15). Here we see a $\varepsilon \propto \bar{U}^3$ dependence that is again suggestive of bottom
475 boundary layer physics (Trowbridge 1992; Nash et al. 2009). At lower flow speeds, ε deviates
476 from this relationship, which suggests that the boundary layer is no longer the dominant physical
477 process at the depth of these measurements.

478 There are two intriguing differences between the ebb and flood datasets: 1) the drag coefficient
479 relating ε to \bar{U}^3 is larger for ebbs, and 2) the fit does not hold as well for low flow speeds (Figure
480 15). These details are not surprising considering the complex bathymetry at the test site (Figure
481 1). In particular, the flow immediately upstream of the measurement site is exposed to much
482 more bathymetric curvature—i.e. from the headland—during ebb (when \bar{u} is > 0) than the during
483 flood ($\bar{u} < 0$). Based on this, one might expect flow separation (turbulence advection), turbulence

484 production, or turbulence transport emanating from the headland to have a stronger impact on
485 the flow at this site during ebb than flood. These effects are a likely contributor to the distinct
486 relationships observed in Figure 15.

487 The hypothesis that the headland is a key contributor to the turbulence dynamics at this site
488 suggests that terms such as cross-stream turbulence advection, $\bar{v}\partial\text{tke}/\partial y$, the lateral turbulent
489 transport terms, $\partial\bar{u}_i\bar{u}_i\bar{v}/\partial y$, or lateral shear production, $\bar{u}\bar{v}\partial\bar{u}/\partial y$, may contribute significantly to
490 the dynamics of turbulence at this site. While we did not measure stratification profiles during
491 these measurements, we do not typically expect buoyancy flux to play dominant role due to the
492 fact that this region tends to be tidally well-mixed (Geyer and Cannon 1982). In summary, bottom
493 boundary layer physics seems to be the dominant process at the measurement site, with lateral
494 advection, lateral transport, and lateral production of tke also potentially contributing—especially
495 during ebb. A more detailed analysis of the turbulence and momentum dynamics of this headland
496 is left for future work (e.g., Warner et al. 2013).

497 6. Conclusion

498 This work presents a methodology for measuring turbulence from moored ADV-IMUs and
499 demonstrates that motion correction reduces mooring motion-contamination. Comparison of spec-
500 tra of ADV head motion, $S\{\vec{u}_h\}$, to that of motion-corrected, $S\{\vec{u}\}$, and uncorrected spectra,
501 $S\{\vec{u}_m\}$, reveals that motion correction improves spectral estimates of moored ADV measurements.
502 In particular, we found that motion-corrected spectra have spectral shapes that are similar to previ-
503 ous measurements of tidal-channel turbulence and have a $f^{-5/3}$ spectral slope at high frequencies.
504 This finding suggests that the motion-corrected spectra resolve the inertial subrange predicted by
505 Kolmogorov’s theory of locally isotropic turbulence.

506 Motion correction reduces motion contamination for all platforms we presented but it does not
507 necessarily remove it completely. This outcome seems to depend on the relative amplitude of plat-
508 form motion compared to the underlying turbulence being measured. The most notable example
509 of this is from the TTM v -component spectra, which have a large-amplitude “swaying” peak at
510 0.15 Hz that interrupts the often observed ‘roll-off’ between the low-frequency ‘energy containing
511 scales’ and the $f^{-5/3}$ inertial subrange.

512 This inconsistency indicates that turbulence measurements from moored, motion-corrected
513 ADV-IMUs must be interpreted with care. An inspection of spectra presented here suggests that
514 excluding spectral regions where $S\{\vec{u}_h\}/S\{\vec{u}\} > 3$ removes persistent-motion contamination peaks
515 while still preserving spectral regions where motion correction is effective. Using this criteria, it
516 is then possible to produce spectral fits that exclude persistent-motion contamination, and provide
517 reliable estimates of turbulence quantities of interest (e.g., ε and tke).

518 We have also shown that motion correction reduces motion contamination in cross spectra. This
519 finding is important because it suggests that moored ADV-IMU measurements may be used to
520 produce reliable estimates of Reynolds stresses. We utilized these stress estimates and vertical
521 shear estimates, both from the TTM, to estimate P_{uz} .

522 Finally, we have shown that ε estimates based on motion-corrected spectra scale with the U^3 ,
523 and balance P_{uz} estimates during peak ebb and flood. Together, these results indicate that bottom
524 boundary layer physics are a dominant process at this site, and that the boundary layer reaches the
525 height of the ADV-IMUs (10 m) during ebb and flood. The degree of agreement between P_{uz} and ε
526 also serves as an indicator of the self-consistency of moored ADV-IMU turbulence measurements.

527 *Acknowledgments.* Many thanks to Joe Talbert, Alex DeKlerk, Captain Andy Reay-Ellers, Jen-
528 nifer Rinker, Maricarmen Guerra, and Eric Nelson in assisting with data collection. The authors

529 are also grateful to James VanZwieten, Matthew Egeland and Marshall Richmond for discussion
530 on the details of this work.

531 Thanks to the open-source software community for the tools used in this work, especially the
532 developers of L^AT_EX, Python, NumPy, Matplotlib, git, and GNU emacs.

533 This work was supported by the U.S. Department of Energy under Contract No. DE-AC36-
534 08GO28308 with the National Renewable Energy Laboratory. Funding for the work was provided
535 by the DOE Office of Energy Efficiency and Renewable Energy, Wind and Water Power Technolo-
536 gies Office.

537 The U.S. Government retains and the publisher, by accepting the article for publication, ac-
538 knowledges that the U.S. Government retains a nonexclusive, paid-up, irrevocable, worldwide
539 license to publish or reproduce the published form of this work, or allow others to do so, for U.S.
540 Government purposes.

541 **References**

- 542 Afgan, I., J. McNaughton, S. Rolfo, D. Apsley, T. Stallard, and P. Stansby, 2013: Turbulent flow
543 and loading on a tidal stream turbine by les and rans. *International Journal of Heat and Fluid*
544 *Flow*, **43**, 96–108.
- 545 Alexander, S. R., and P. E. Hamlington, 2015: Analysis of turbulent bending moments in tidal
546 current boundary layers. *Journal of Renewable and Sustainable Energy*, **7 (6)**, 063 118.
- 547 Alford, M. H., 2010: Sustained, full-water-column observations of internal waves and mixing near
548 mendocino escarpment. *Journal of Physical Oceanography*, **40 (12)**, 2643–2660, doi:10.1175/
549 2010JPO4502.1.
- 550 Axford, D., 1968: On the accuracy of wind measurements using an inertial platform in an aircraft,
551 and an example of a measurement of the vertical mesostructure of the atmosphere. *Journal of*
552 *Applied Meteorology*, **7 (4)**, 645–666.
- 553 Barshan, B., and H. F. Durrant-Whyte, 1995: Inertial navigation systems for mobile robots. *IEEE*
554 *Transactions on Robotics and Automation*, **11 (3)**, 328–342.
- 555 Bevly, D. M., 2004: Global positioning system (gps): A low-cost velocity sensor for correcting in-
556 erial sensor errors on ground vehicles. *Journal of dynamic systems, measurement, and control*,
557 **126 (2)**, 255–264.
- 558 Cartwright, G. M., C. T. Friedrichs, P. J. Dickhudt, T. Gass, and F. H. Farmer, 2009: Using the
559 acoustic doppler velocimeter (adv) in the mudbed real-time observing system. *Marine Technol-
560 ogy for Our Future: Global and Local Challenges*.
- 561 Doherty, K., D. Frye, S. Liberatore, and J. Toole, 1999: A moored profiling instrument*. *Journal*
562 *of Atmospheric and Oceanic Technology*, **16 (11)**, 1816–1829.

- 563 Edson, J. B., A. A. Hinton, K. E. Prada, J. E. Hare, and C. W. Fairall, 1998: Direct covariance
564 flux estimates from mobile platforms at sea*. *Journal of Atmospheric and Oceanic Technology*,
565 **15** (2), 547–562, doi:10.1175/1520-0426(1998)015<0547:DCFEFM>2.0.CO;2.
- 566 Egeland, M. N., 2014: Spectral evaluation of motion compensated ADV systems for ocean turbu-
567 lence measurements. Ph.D. thesis, Florida Atlantic University.
- 568 Fer, I., and M. B. Paskyabi, 2014: Autonomous ocean turbulence measurements using shear probes
569 on a moored instrument. *Journal of Atmospheric and Oceanic Technology*, **31** (2), 474–490, doi:
570 10.1175/JTECH-D-13-00096.1.
- 571 Finlayson, D., 2005: Combined bathymetry and topography of the Puget Lowlands, Washington
572 state. URL <http://www.ocean.washington.edu/data/pugetsound/>.
- 573 Geyer, R. W., M. E. Scully, and D. K. Ralston, 2008: Quantifying vertical mixing in estuaries.
574 *Environmental Fluid Mechanics*, **8**, 495–509, doi:10.1007/s10652-008-9107-2.
- 575 Geyer, W. R., and G. A. Cannon, 1982: Sill processes related to deep water renewal in a fjord. *Jour-*
576 *nal of Geophysical Research: Oceans*, **87** (C10), 7985–7996, doi:10.1029/JC087iC10p07985.
- 577 Goodman, L., E. R. Levine, and R. G. Lueck, 2006: On measuring the terms of the turbulent
578 kinetic energy budget from an auv. *Journal of Atmospheric and Oceanic Technology*, **23** (7),
579 977–990, doi:10.1175/JTECH1889.1.
- 580 Grant, H. L., R. W. Stewart, and A. Moilliet, 1962: Turbulence spectra from a tidal channel.
581 *Journal of Fluid Mechanics*, **12**, 241–263.
- 582 Gulmammadov, F., 2009: Analysis, modeling and compensation of bias drift in mems inertial
583 sensors. *Recent Advances in Space Technologies, 2009. RAST'09. 4th International Conference*
584 *on*, IEEE, 591–596.

- 585 Gunawan, B., V. S. Neary, and J. Colby, 2014: Tidal energy site resource assessment in the East
586 River tidal strait, near Roosevelt Island, New York, NY (USA). *Renewable Energy*, **71**, 509–
587 517, doi:10.1016/j.renene.2014.06.002.
- 588 Hand, M. M., N. D. Kelley, and M. J. Balas, 2003: Identification of wind turbine response to
589 turbulent inflow structures. Tech. Rep. NREL/CP-500-33465, National Renewable Energy Lab-
590 oratory.
- 591 Harding, S., L. Kilcher, and J. Thomson, 2017: Turbulence measurements from compliant moor-
592 ings - part 1: Motion characterization, in review.
- 593 Kelley, N. D., B. J. Jonkman, G. N. Scott, J. T. Bialasiewicz, and L. S. Redmond, 2005: The impact
594 of coherent turbulence on wind turbine aeroelastic response and its simulation. *WindPower*,
595 Denver, Colorado, NREL/CP-500-38074, may 15-18.
- 596 Kilcher, L., J. Thomson, J. Talbert, and A. DeKlerk, 2016: Measuring turbulence from moored
597 acoustic Doppler velocimeters: A manual to quantifying inflow at tidal energy sites. 9 62979,
598 National Renewable Energy Laboratory. URL www.nrel.gov/docs/fy16osti/62979.pdf.
- 599 Kim, S. C., C. T. Friedrichs, J. P.-Y. Maa, and L. D. Wright, 2000: Estimating bottom stress in
600 tidal boundary layer from acoustic doppler velocimeter data. *Journal of Hydraulic Engineering*,
601 399–406.
- 602 Kolmogorov, A. N., 1941: Dissipation of energy in the locally isotropic turbulence. *Dokl. Akad.*
603 *Nauk SSSR*, **32** (1), 16–18, URL <http://www.jstor.org/stable/51981>.
- 604 Kraus, N. C., A. Lohrmann, and R. Cabrera, 1994: A new acoustic meter for measuring 3D
605 laboratory flows. *Journal of Hydraulic Engineering*, **120**, 406–412.

- 606 Lohrmann, A., R. Cabrera, G. Gelfenbaum, and J. Haines, 1995: Direct measurements of reynolds
607 stress with an acoustic doppler velocimeter. *Current Measurement, 1995.*, *Proceedings of the*
608 *IEEE Fifth Working Conference on*, 205–210, doi:10.1109/CCM.1995.516175.
- 609 Lorke, A., 2007: Boundary mixing in the thermocline of a large lake. *Journal of Geophysical*
610 *Research: Oceans*, **112 (C9)**, n/a–n/a, doi:10.1029/2006JC004008, c09019.
- 611 Lueck, R. G., and D. Huang, 1999: Dissipation measurement with a moored instrument in a swift
612 tidal channel. *Journal of atmospheric and oceanic technology*, **16**, 1499–1505.
- 613 Lumley, J., and E. Terray, 1983: Kinematics of turbulence convected by a random wave field.
614 *Journal of Physical Oceanography*, **13 (11)**, 2000–2007.
- 615 McCaffrey, K., B. Fox-Kemper, P. E. Hamlington, and J. Thomson, 2015: Characterization of
616 turbulence anisotropy, coherence, and intermittency at a prospective tidal energy site: Observa-
617 tional data analysis. *Renewable Energy*, **76**, 441–453.
- 618 McMillan, J. M., A. E. Hay, R. G. Lueck, and F. Wolk, 2016: Rates of dissipation of turbulent
619 kinetic energy in a high reynolds number tidal channel. *Journal of Atmospheric and Oceanic*
620 *Technology*, **33 (4)**, 817–837, doi:10.1175/JTECH-D-15-0167.1.
- 621 MicroStrain, I., 2010: Technical note: Coning and sculling. Tech. Rep. I0019, MicroStrain. URL
622 http://files.microstrain.com/TN-I0019_3DM-GX3-25__Coning_And_Sculling.pdf.
- 623 MicroStrain, I., 2012: *3DM-GX3-15,-25 MIP Data Communications Protocol*. URL <http://files.microstrain.com/3DM-GX3-15-25-MIP-Data-Communications-Protocol.pdf>, retrieved
624 January 2014.

- 626 Miller, S. D., T. S. Hristov, J. B. Edson, and C. A. Friehe, 2008: Platform motion effects on
627 measurements of turbulence and air-sea exchange over the open ocean. *Journal of Atmospheric*
628 and *Oceanic Technology*, **25** (9), 1683–1694, doi:10.1175/2008JTECHO547.1.
- 629 Morison, J. R., J. W. Johnson, and S. A. Schaaf, 1950: The force exerted by surface waves on
630 piles. *Journal of Petroleum Technology*, **2** (05), 149–154.
- 631 Moum, J., and J. Nash, 2009: Mixing measurements on an equatorial ocean mooring. *Journal of*
632 *Atmospheric and Oceanic Technology*, **26** (2), 317–336.
- 633 Mücke, T., D. Kleinhans, and J. Peinke, 2011: Atmospheric turbulence and its influence on the
634 alternating loads on wind turbines. *Wind Energy*, **14**, 301–316.
- 635 Nash, J. D., L. F. Kilcher, and J. N. Moum, 2009: Structure and composition of a strongly
636 stratified, tidally pulsed river plume. *Journal of Geophysical Research*, **114**, C00B12, doi:
637 10.1029/2008JC005036.
- 638 Nash, J. D., E. Kunze, J. M. Toole, and R. W. Schmitt, 2004: Internal tide reflection and turbulent
639 mixing on the continental slope. *Journal of Physical Oceanography*, **34** (5), 1117–1134, doi:
640 10.1175/1520-0485(2004)034<1117:ITRATM>2.0.CO;2.
- 641 Nortek, 2005: *Vector Current Meter User Manual*. Vangkroken 2, NO-1351 RUD, Norway, h ed.
- 642 Paskyabi, M. B., and I. Fer, 2013: Turbulence measurements in shallow water from a subsurface
643 moored moving platform. *Energy Procedia*, **35**, 307 – 316, doi:10.1016/j.egypro.2013.07.183.
- 644 Perlin, A., and J. N. Moum, 2012: Comparison of thermal variance dissipation rates from moored
645 and profiling instruments at the equator. *Journal of Atmospheric and Oceanic Technology*.

- 646 Polagye, B., and J. Thomson, 2013: Tidal energy resource characterization: methodology and field
647 study in admiralty inlet, Puget Sound, WA (USA). *Proceedings of the Institution of Mechanical*
648 *Engineers, Part A: Journal of Power and Energy*, **227** (3), 352–367.
- 649 Rippeth, T. P., E. Williams, and J. H. Simpson, 2002: Reynolds stress and turbulent en-
650 ergy production in a tidal channel. *Journal of Physical Oceanography*, **32**, 1242–1251, doi:
651 10.1175/1520-0485(2002)032\$(\$1242:RSATEP\$)\$2.0.CO;2.
- 652 Sreenivasan, K. R., 1995: On the universality of the Kolmogorov constant. *Physics of Fluids*, **7**,
653 2778–2784.
- 654 Stacey, M. T., S. G. Monismith, and J. R. Burau, 1999a: Measurements of reynolds stress
655 profiles in unstratified tidal flow. *J. Geophys. Res.*, **104** (C5), 10 933–10 949, doi:10.1029/
656 1998JC900095.
- 657 Stacey, M. T., S. G. Monismith, and J. R. Burau, 1999b: Observations of turbulence in a partially
658 stratified estuary. *Journal of Physical Oceanography*, **29**, 1950–1970.
- 659 Thomson, J., B. Polagye, V. Durgesh, and M. Richmond, 2012: Measurements of turbulence at
660 two tidal energy sites in Puget Sound, WA. *Journal of Oceanic Engineering*, **37** (3), 363–374,
661 doi:10.1109/JOE.2012.2191656.
- 662 Trowbridge, J. H., 1992: A simple description of the deepening and structure of a stably stratified
663 flow driven by a surface stress. *Journal of Geophysical Research*, **97**, 15 529–15 543.
- 664 Trowbridge, J. H., W. R. Geyer, M. M. Bowen, and A. J. I. Williams, 1999: Near-bottom turbu-
665 lence measurements in a partially mixed estuary: turbulent energy balance, velocity structure
666 and along-channel momentum balance. *Journal of Physical Oceanography*, **29**, 3056–3072.

- van der Walt, S., S. C. Colbert, and G. Varoquaux, 2011: The numpy array: A structure for efficient numerical computation. *Computing in Science & Engineering*, **13**, 22–30, doi:10.1109/MCSE.2011.37.
- VanZwieten, J. H., M. N. Egeland, K. D. von Ellenrieder, J. W. Lovenbury, and L. Kilcher, 2015: Experimental evaluation of motion compensated adv measurements for in-stream hydrokinetic applications. *Current, Waves and Turbulence Measurement (CWTM), 2015 IEEE/OES Eleventh*, 1–8, doi:10.1109/CWTM.2015.7098119.
- Voulgaris, G., and J. H. Trowbridge, 1998: Evaluation of the acoustic doppler velocimeter (adv) for turbulence measurements. *Journal of Atmospheric and Oceanic technology*, **15**, 272–289.
- Walter, R. K., N. J. Nidzieko, and S. G. Monismith, 2011: Similarity scaling of turbulence spectra and cospectra in a shallow tidal flow. *Journal of Geophysical Research: Oceans*, **116 (C10)**.
- Warner, S. J., P. MacCready, J. N. Moum, and J. D. Nash, 2013: Measurement of tidal form drag using seafloor pressure sensors. *Journal of Physical Oceanography*, **43 (6)**, 1150–1172.
- Wiles, P. J., T. P. Rippeth, J. H. Simpson, and P. J. Hendricks, 2006: A novel technique for measuring the rate of turbulent dissipation in the marine environment. *Geophysical Research Letters*, **33**, 21 608.
- Winkel, D., M. Gregg, and T. Sanford, 1996: Resolving oceanic shear and velocity with the multi-scale profiler. *Journal of Atmospheric and Oceanic Technology*, **13 (5)**, 1046–1072.
- Wyngaard, J. C., L. Rockwell, and C. A. Friehe, 1985: Errors in the measurement of turbulence upstream of an axisymmetric body. *Journal of Atmospheric and Oceanic Technology*, **2 (4)**, 605–614.

688 Zhang, Y., K. Streitlien, J. G. Bellingham, and A. B. Baggeroer, 2001: Acoustic doppler ve-
689 locimeter flow measurement from an autonomous underwater vehicle with applications to deep
690 ocean convection. *Journal of Atmospheric and Oceanic Technology*, **18** (12), 2038–2051, doi:
691 10.1175/1520-0426(2001)018<2038:ADVFMF>2.0.CO;2.

692 LIST OF FIGURES

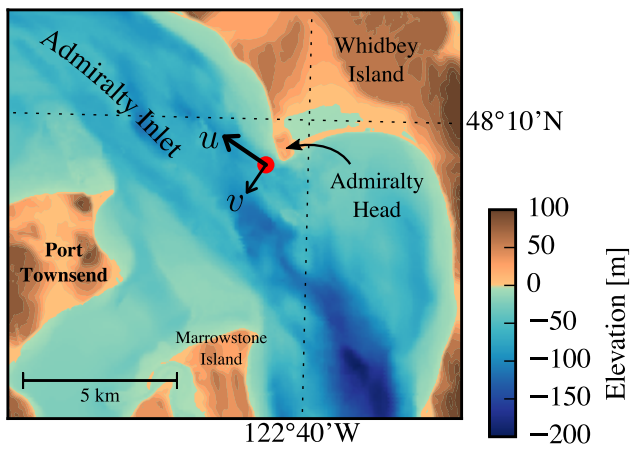
693	Fig. 1.	Bathymetry of Admiralty Inlet near Port Townsend, Washington, U.S.A. (Finlayson 2005). The red dot indicates the location of all measurements. The positive u direction is the direction of ebb flow (thick arrow originating from red dot), and positive v is away from Admiralty Head (smaller arrow).	36
697	Fig. 2.	Schematic diagram of the TTM; not to scale.	37
698	Fig. 3.	TTM components on the deck of the R/V Jack Robertson. The TTM includes two ADVs, with pressure cases mounted on opposite sides of the fin. The anchor stack includes a pop-up buoy for retrieval. The green arrow indicates the vector from the IMU to the ADV head (face of the transmit transducer).	38
702	Fig. 4.	Top: Alex DeKlerk checks to ensure that the StableMoor buoy is properly fastened to its anchor; the RDI workhorse ADCP can be seen in the rear instrument bay. A bridle is draped across the top of the buoy for deployment and recovery, and a small marker buoy fastened to the tail is useful during recovery. Bottom: a close-up of the StableMoor buoy with the ADV head and the top of its pressure case. The green arrow indicates the vector from the IMU to the ADV head.	39
708	Fig. 5.	The turbulence platform showing details of the ADV head and pressure case configuration. The green arrow indicates the vector from the IMU to the ADV head. The head cable was taped out of the way beneath the sounding weight tail fins shortly after taking this photo.	40
711	Fig. 6.	The spectral noise levels of rotational velocity ($S\{\vec{n}_\omega\}$, yellow) and translational velocity ($S\{\vec{n}_a\}$, black) estimated from an ADV-IMU resting motionless on a table. Solid and dashed lines indicate the horizontal and vertical components, respectively, of $S\{\vec{n}_a\}$ and $S\{\vec{u}_{low}\}$. The horizontal components are equivalent, as are all three components of $S\{\vec{n}_\omega\}$. The \vec{n}_a signals are unfiltered (black), and high-pass filtered at 30 s (purple) and 5 s (green); vertical dotted lines indicate the filter frequency. Blue lines are an estimate of \vec{u}_{low} for the TTM. The horizontal and vertical Doppler noise levels of a Nortek Vector ADV configured to measure ± 4 m/s are indicated by horizontal dash-dot and dotted lines, respectively. The shaded region indicates the range of u spectral amplitudes presented herein ($0.002 < \text{tke} < 0.03 \text{ m}^2/\text{s}^2$, $1\text{e}-5 < \varepsilon < 5\text{e}-4 \text{ W/kg}$).	41
721	Fig. 7.	Motion-corrected velocity spectra, $S\{\vec{u}\}$, for a range of high-pass filter frequencies: $f_a = 0.33 \text{ Hz}$ (red), 0.033 Hz (thick black), and 0.0033 Hz (cyan). The vertical dashed lines indicate the filter frequency. The thick grey line is $S\{\vec{u}_h\}$ for $f_a = 0.0033 \text{ Hz}$. The data are from the June 2014 TTM deployment when $2.0 < \vec{u} < 2.5 \text{ ms}^{-1}$.	42
725	Fig. 8.	Time series of tidal velocity at Admiralty Head from ADV-IMU measurements (black), and an acoustic Doppler profiler on the anchor (red). The profiler measurements—taken at the same depth as the ADV on the TTM—were contaminated by acoustic reflection from the strongback fin when it was inline with one of the profiler’s beams. Note that the vertical scale on the three axes vary by more than an order of magnitude; the small ticks in A and B are equivalent to the ticks in C.	43
731	Fig. 9.	Turbulence spectra from the June 2014 TTM deployment. Each column is for a range of streamwise velocity magnitudes (indicated at top). The rows are for each component of velocity (indicated to the lower right of the right column). The uncorrected spectra are in black and the corrected spectra are blue, and the spectra of ADV head motion, \vec{u}_h , is red (also indicated in the legend). The vertical red dotted line indicates the filter frequency applied	

Fig. 10. Turbulence spectra from the StableMoor buoy. The axes layout and annotations are identical to Figure 9, except that $S\{\vec{u}_h\}$ is plotted as a solid line at all frequencies because it is measured at all frequencies. 45

Fig. 12. Variance preserving cross-spectra between components of \vec{u} (blue), \vec{u}_h (red), and \vec{u}_m (black) from the June 2014 TTM deployment. The upper row is $f \cdot C\{u, v\}$, the middle row is $f \cdot C\{u, w\}$, and the bottom row is $f \cdot C\{v, w\}$. Note that these cross-spectra are between components of a velocity vector (e.g., \vec{u}), not between different vectors (i.e., not between \vec{u} and \vec{u}_m). The columns are for different ensemble-averages over distinct ranges of the stream-wise mean velocity magnitude (indicated above the top row). N is the number of spectral ensembles in each column. The light blue shading indicates one standard deviation of $f \cdot C\{\vec{u}\}$. The number in the lower-right corner of each panel indicates the ensemble-averaged estimate of the Reynold's stress component (integral of the blue line) in units of $10^{-3} \text{ m}^2 \text{s}^{-2}$.

Fig. 14. P_{uz} vs. ϵ during the June 2014 TTM deployment for values of $|u| > 1$ m/s. Values of negative production are indicated as open circles. 49

Fig. 15. A log-log plot of ε vs. \bar{U} for the June 2014 TTM (diamonds) and May 2015 StableMoor (dots) deployments, during ebb (left) and flood (right). Black points are 5-minute averages. Green dots are mean values within speed bins of 0.2 m s^{-1} width that have at least 10 points (50 minutes of data); their vertical bars are 95% bootstrap confidence intervals. The blue line shows a U^3 slope, wherein the proportionality constant (blue box) is calculated by taking the log-space mean of ε/U^3 . 50



766 FIG. 1. Bathymetry of Admiralty Inlet near Port Townsend, Washington, U.S.A. (Finlayson 2005). The red
 767 dot indicates the location of all measurements. The positive u direction is the direction of ebb flow (thick arrow
 768 originating from red dot), and positive v is away from Admiralty Head (smaller arrow).

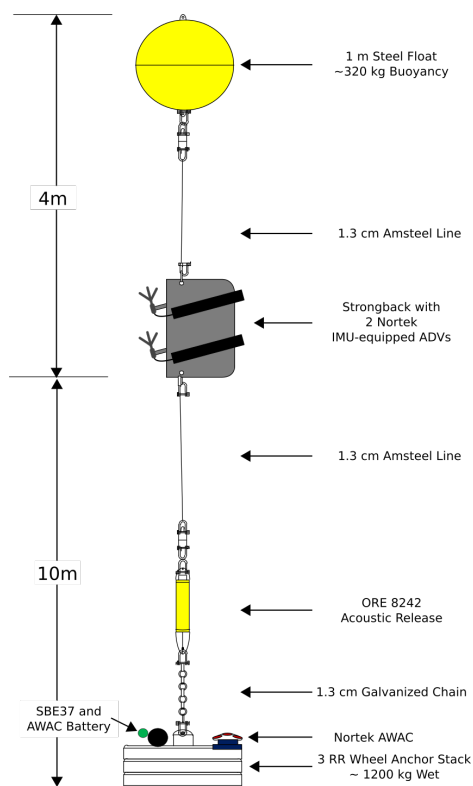
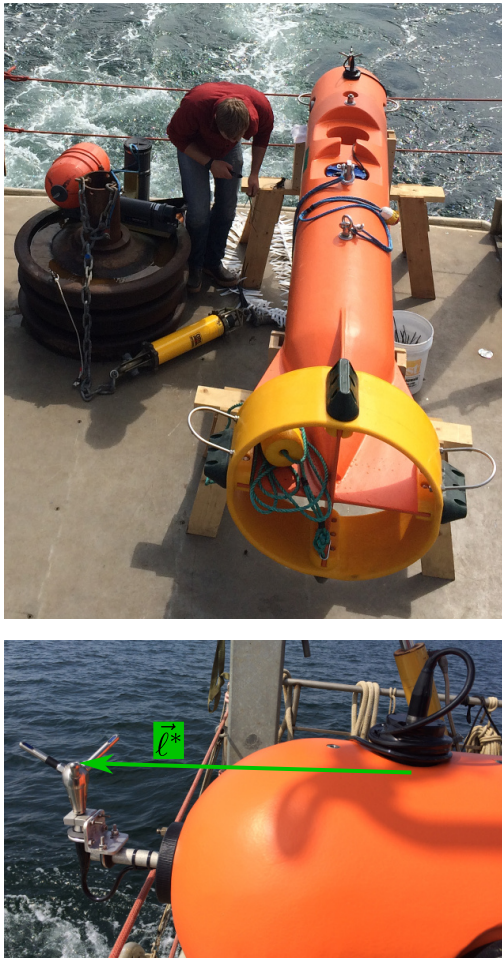


FIG. 2. Schematic diagram of the TTM; not to scale.



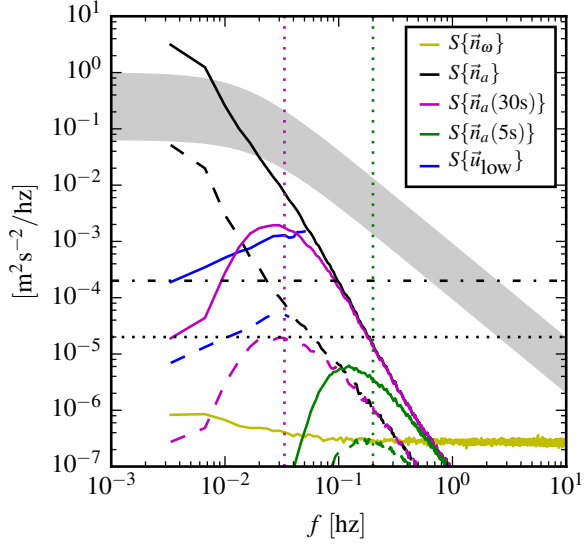
769 FIG. 3. TTM components on the deck of the R/V Jack Robertson. The TTM includes two ADVs, with
770 pressure cases mounted on opposite sides of the fin. The anchor stack includes a pop-up buoy for retrieval. The
771 green arrow indicates the vector from the IMU to the ADV head (face of the transmit transducer).



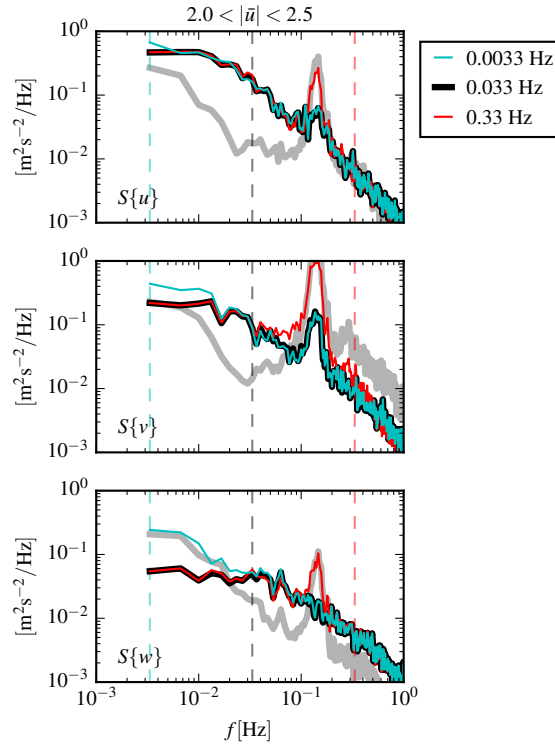
772 FIG. 4. Top: Alex DeKlerk checks to ensure that the StableMoor buoy is properly fastened to its anchor; the
 773 RDI workhorse ADCP can be seen in the rear instrument bay. A bridle is draped across the top of the buoy
 774 for deployment and recovery, and a small marker buoy fastened to the tail is useful during recovery. Bottom: a
 775 close-up of the StableMoor buoy with the ADV head and the top of its pressure case. The green arrow indicates
 776 the vector from the IMU to the ADV head.



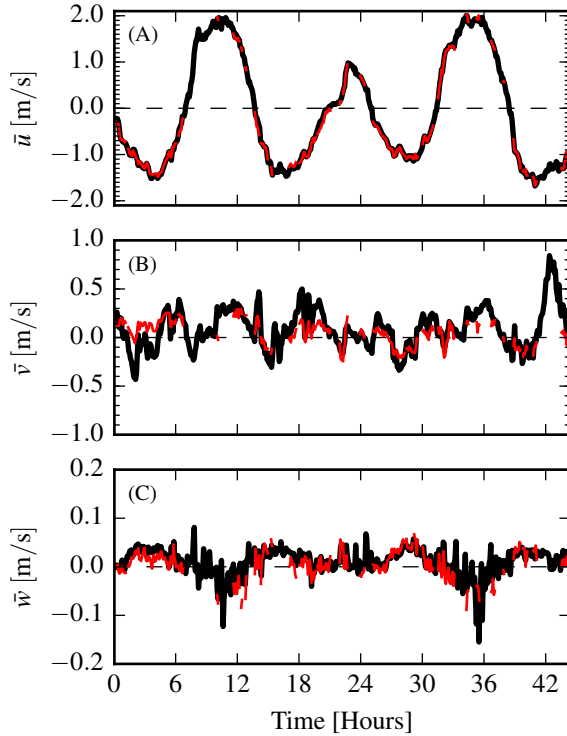
777 FIG. 5. The turbulence platform showing details of the ADV head and pressure case configuration. The green
778 arrow indicates the vector from the IMU to the ADV head. The head cable was taped out of the way beneath the
779 sounding weight tail fins shortly after taking this photo.



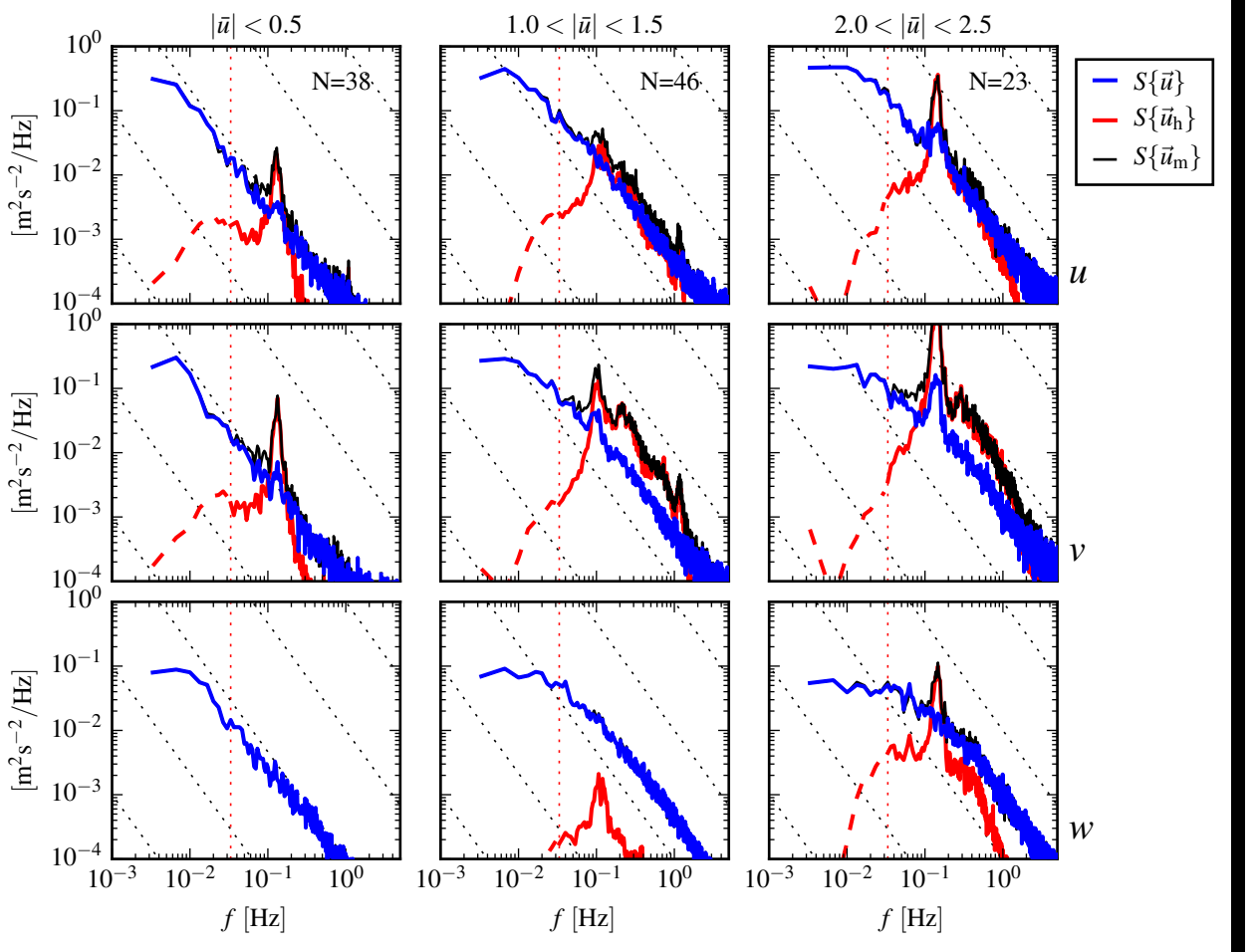
780 FIG. 6. The spectral noise levels of rotational velocity ($S\{\vec{n}_\omega\}$, yellow) and translational velocity ($S\{\vec{n}_a\}$,
 781 black) estimated from an ADV-IMU resting motionless on a table. Solid and dashed lines indicate the horizontal
 782 and vertical components, respectively, of $S\{\vec{n}_a\}$ and $S\{\vec{u}_{\text{low}}\}$. The horizontal components are equivalent, as are
 783 all three components of $S\{\vec{n}_\omega\}$. The \vec{n}_a signals are unfiltered (black), and high-pass filtered at 30 s (purple)
 784 and 5 s (green); vertical dotted lines indicate the filter frequency. Blue lines are an estimate of \vec{u}_{low} for the
 785 TTM. The horizontal and vertical Doppler noise levels of a Nortek Vector ADV configured to measure $\pm 4 \text{ m/s}$
 786 are indicated by horizontal dash-dot and dotted lines, respectively. The shaded region indicates the range of u
 787 spectral amplitudes presented herein ($0.002 < \text{tke} < 0.03 \text{ m}^2/\text{s}^2$, $1\text{e}-5 < \varepsilon < 5\text{e}-4 \text{ W/kg}$).



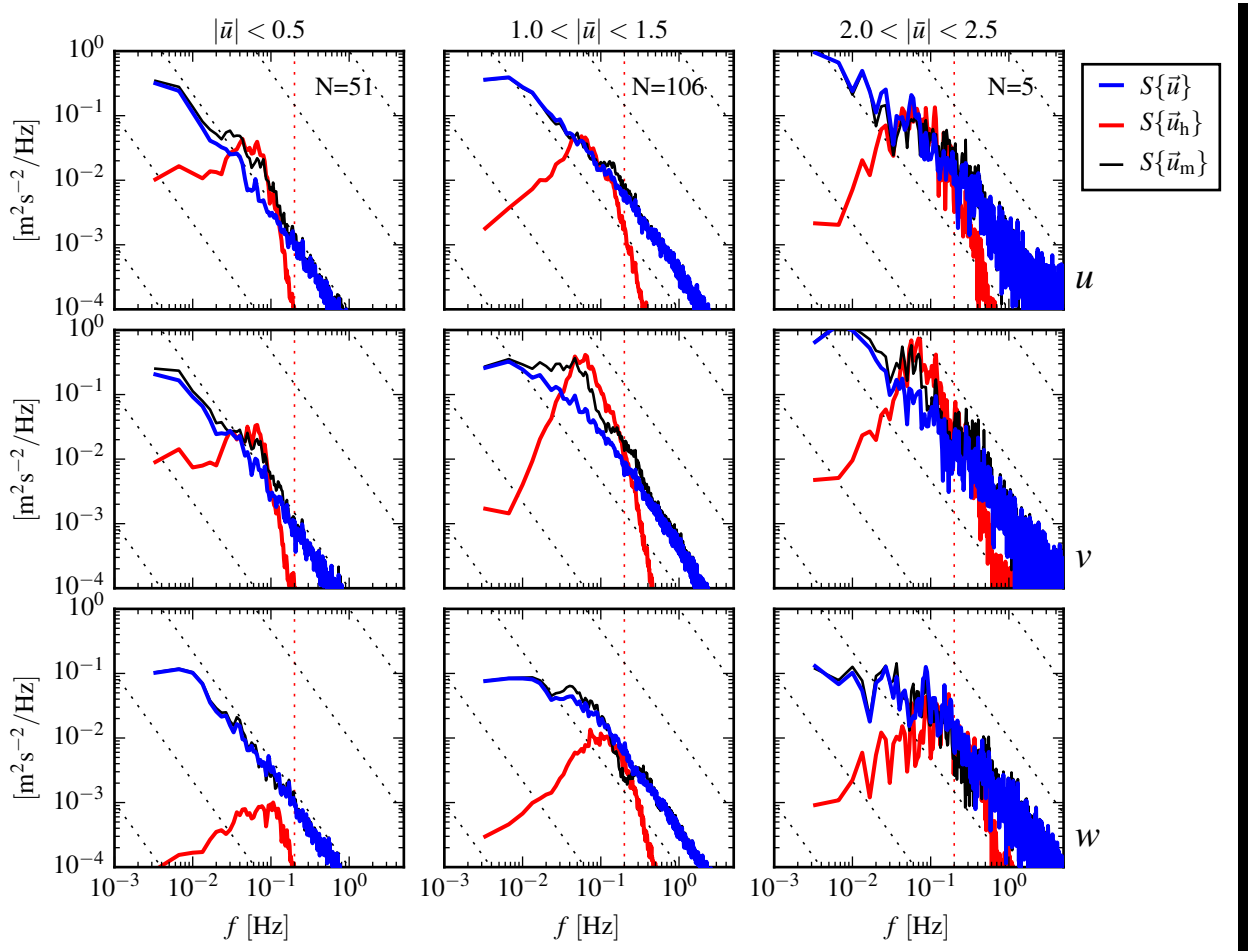
788 FIG. 7. Motion-corrected velocity spectra, $S\{\vec{u}\}$, for a range of high-pass filter frequencies: $f_a = 0.33$ Hz
 789 (red), 0.033 Hz (thick black), and 0.0033 Hz (cyan). The vertical dashed lines indicate the filter frequency.
 790 The thick grey line is $S\{\vec{u}_h\}$ for $f_a = 0.0033$ Hz. The data are from the June 2014 TTM deployment when
 791 $2.0 < |\bar{u}| < 2.5 \text{ ms}^{-1}$.



792 FIG. 8. Time series of tidal velocity at Admiralty Head from ADV-IMU measurements (black), and an acoustic
 793 Doppler profiler on the anchor (red). The profiler measurements—taken at the same depth as the ADV on the
 794 TTM—were contaminated by acoustic reflection from the strongback fin when it was inline with one of the
 795 profiler’s beams. Note that the vertical scale on the three axes vary by more than an order of magnitude; the
 796 small ticks in A and B are equivalent to the ticks in C.



797 FIG. 9. Turbulence spectra from the June 2014 TTM deployment. Each column is for a range of streamwise
 798 velocity magnitudes (indicated at top). The rows are for each component of velocity (indicated to the lower right
 799 of the right column). The uncorrected spectra are in black and the corrected spectra are blue, and the spectra
 800 of ADV head motion, \vec{u}_h , is red (also indicated in the legend). The vertical red dotted line indicates the filter
 801 frequency applied to the IMU accelerometers when estimating \vec{u}_h ; below this frequency $S\{\vec{u}_h\}$ is plotted as a
 802 dashed line. Diagonal black dotted lines indicate a $f^{-5/3}$ slope. The number of spectral ensembles, N , in each
 803 column is indicated in the top row.



804 FIG. 10. Turbulence spectra from the StableMoor buoy. The axes layout and annotations are identical to
 805 Figure 9, except that $S\{\vec{u}_h\}$ is plotted as a solid line at all frequencies.

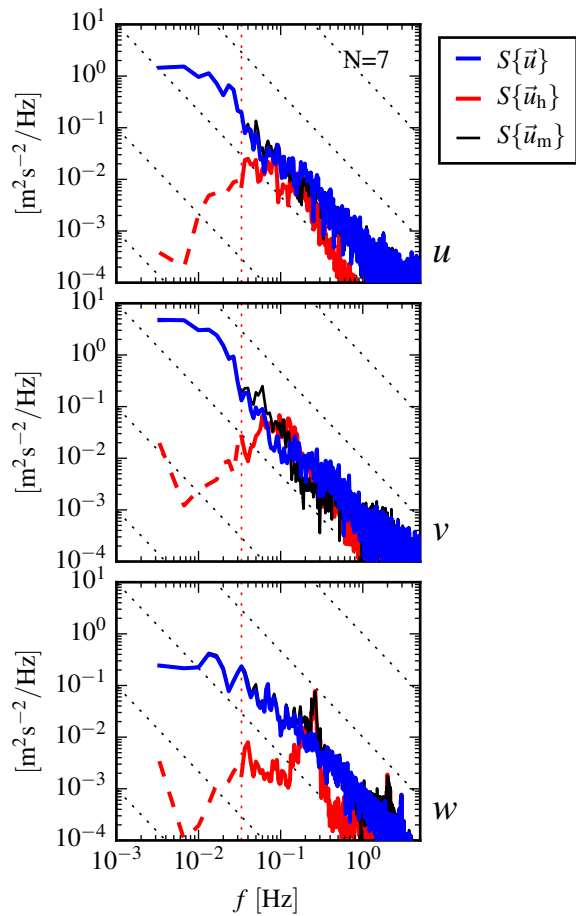


FIG. 11. Turbulence spectra from the turbulence torpedo during a 35-minute period when the mean velocity was 1.3 m/s. Annotations and line colors are identical to Figure 9.

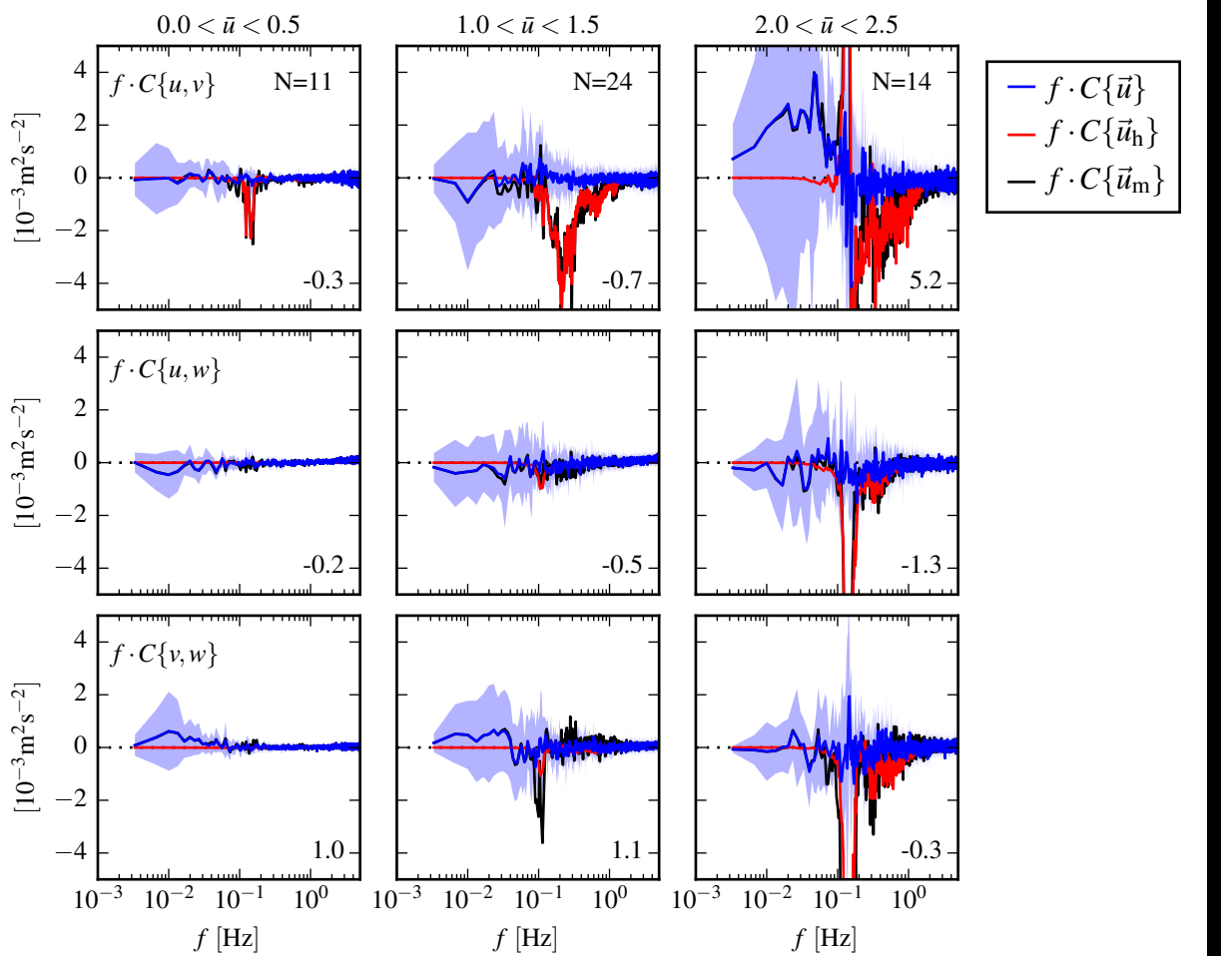


FIG. 12. Variance preserving cross-spectra between components of \vec{u} (blue), \vec{u}_h (red), and \vec{u}_m (black) from the June 2014 TTM deployment. The upper row is $f \cdot C\{u, v\}$, the middle row is $f \cdot C\{u, w\}$, and the bottom row is $f \cdot C\{v, w\}$. Note that these cross-spectra are between components of a velocity vector (e.g., \vec{u}), not between different vectors (i.e., not between \vec{u} and \vec{u}_m). The columns are for different ensemble-averages over distinct ranges of the stream-wise mean velocity magnitude (indicated above the top row). N is the number of spectral ensembles in each column. The light blue shading indicates one standard deviation of $f \cdot C\{\vec{u}\}$. The number in the lower-right corner of each panel indicates the ensemble-averaged estimate of the Reynold's stress component (integral of the blue line) in units of $10^{-3} \text{ m}^2 \text{s}^{-2}$.

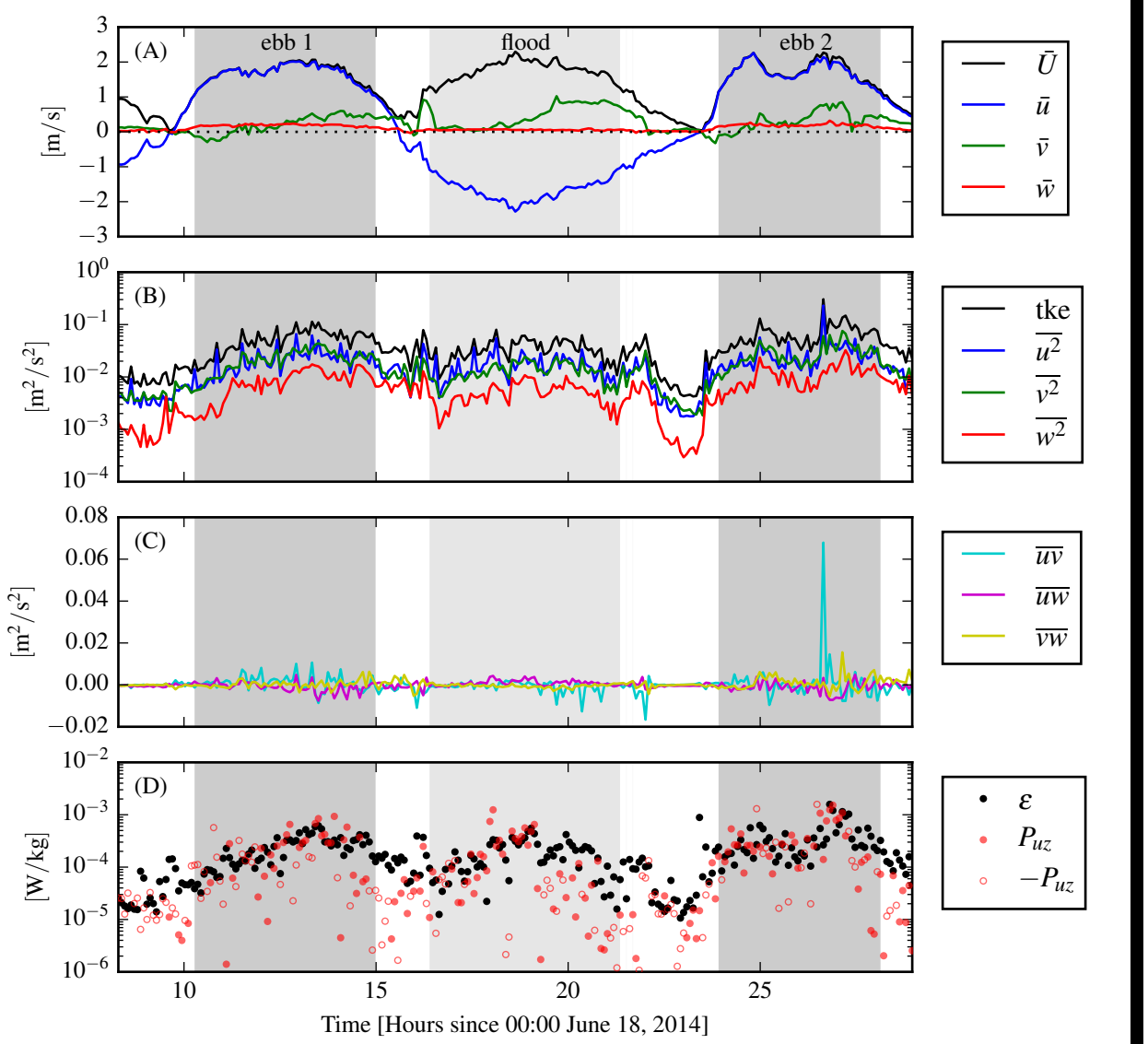
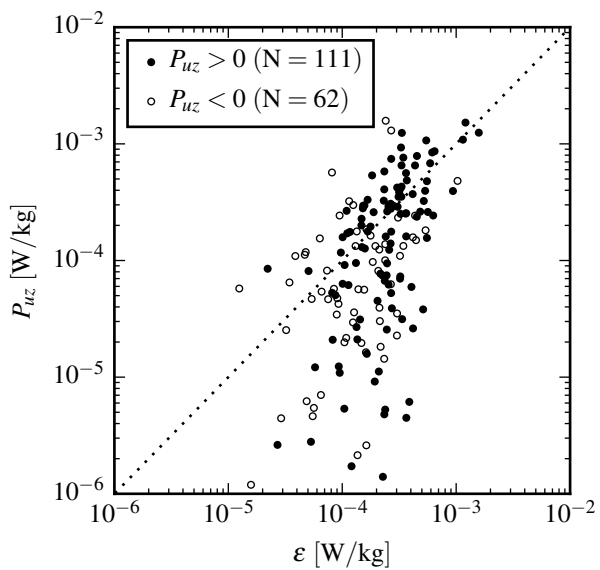
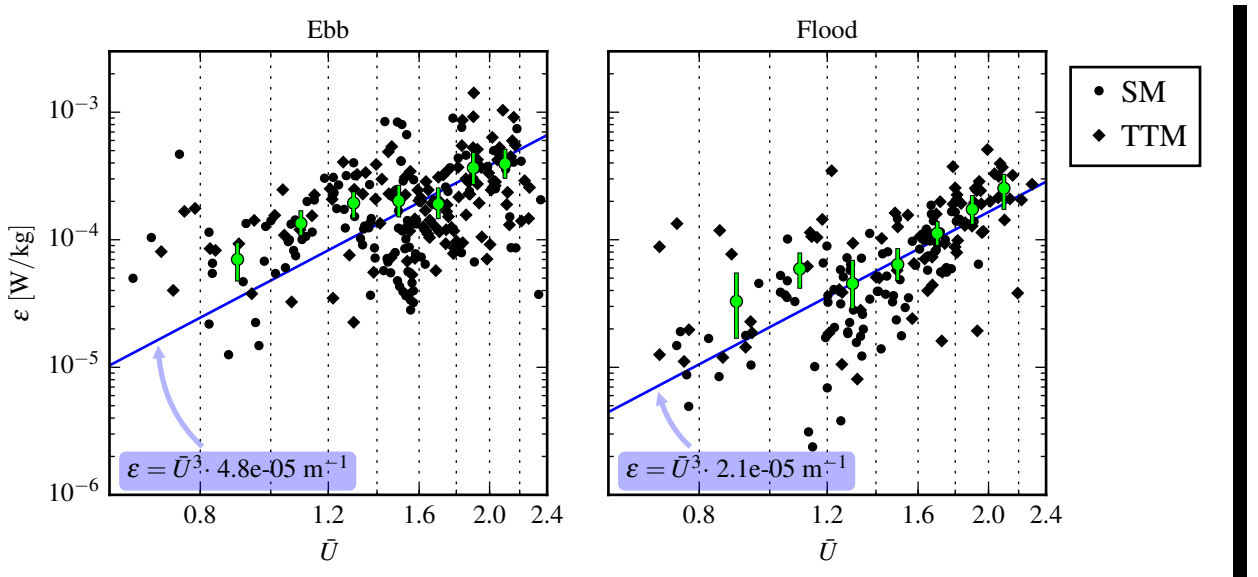


FIG. 13. Time series of mean velocities (A), turbulence energy and its components (B), Reynold's stresses (C), and turbulence dissipation rate (D) measured by the TTM during the June 2014 deployment. Shading indicates periods of ebb ($\bar{u} > 1.0 \text{ ms}^{-1}$, grey) and flood ($\bar{u} < -1.0 \text{ ms}^{-1}$, lighter grey).



819 FIG. 14. P_{uz} vs. ϵ during the June 2014 TTM deployment for values of $|u| > 1$ m/s. Values of negative
820 production are indicated as open circles.



821 FIG. 15. A log-log plot of ε vs. \bar{U} for the June 2014 TTM (diamonds) and May 2015 StableMoor (dots)
822 deployments, during ebb (left) and flood (right). Black points are 5-minute averages. Green dots are mean
823 values within speed bins of 0.2 m s^{-1} width that have at least 10 points (50 minutes of data); their vertical bars
824 are 95% bootstrap confidence intervals. The blue line shows a U^3 slope, wherein the proportionality constant
825 (blue box) is calculated by taking the log-space mean of ε/U^3 .